

# Altered hemodynamics and vascular reactivity in a mouse model with severe pericyte deficiency

Jillian L Stobart<sup>1,2,3</sup> , Eva Erlebach<sup>1,2</sup>, Chaim Glück<sup>1,2</sup> , Sheng-Fu Huang<sup>2,4</sup>, Matthew JP Barrett<sup>1,2</sup>, Max Li<sup>1,2</sup>, Sergei A Vinogradov<sup>5</sup>, Jan Klohs<sup>2,6</sup>, Yvette Zarb<sup>2,4</sup> , Annika Keller<sup>2,4</sup>  and Bruno Weber<sup>1,2</sup>

Journal of Cerebral Blood Flow & Metabolism  
2023, Vol. 43(5) 763–777  
© The Author(s) 2022



Article reuse guidelines:  
sagepub.com/journals-permissions  
DOI: 10.1177/0271678X221147366  
journals.sagepub.com/home/jcbfm



## Abstract

Pericytes are the mural cells of the microvascular network that are in close contact with underlying endothelial cells. Endothelial-secreted PDGFB leads to recruitment of pericytes to the vessel wall, but this is disrupted in *Pdgfb*<sup>ret/ret</sup> mice when the PDGFB retention motif is deleted. This results in severely reduced pericyte coverage on blood vessels. In this study, we investigated vascular abnormalities and hemodynamics in *Pdgfb*<sup>ret/ret</sup> mice throughout the cerebrovascular network and in different cortical layers by *in vivo* two-photon microscopy. We confirmed that *Pdgfb*<sup>ret/ret</sup> mice are severely deficient in pericytes throughout the vascular network, with enlarged brain blood vessels and a reduced number of vessel branches. Red blood cell velocity, linear density, and tube hematocrit were reduced in *Pdgfb*<sup>ret/ret</sup> mice, which may impair oxygen delivery to the tissue. We also measured intravascular PO<sub>2</sub> and found that concentrations were higher in cortical Layer 2/3 in *Pdgfb*<sup>ret/ret</sup> mice, indicative of reduced blood oxygen extraction. Finally, we found that *Pdgfb*<sup>ret/ret</sup> mice had a reduced capacity for vasodilation in response to an acetazolamide challenge during functional MRI imaging. Taken together, these results suggest that severe pericyte deficiency can lead to vascular abnormalities and altered cerebral blood flow, reminiscent of pathologies such as arteriovenous malformations.

## Keywords

Pericytes, brain vasculature, hemodynamics, blood oxygen, vascular reactivity

Received 15 July 2022; Revised 18 October 2022; Accepted 11 November 2022

## Introduction

Pericytes are vascular mural cells in close contact with endothelial cells on capillaries. Brain pericytes have essential roles in angiogenesis,<sup>4</sup> maintenance of the blood-brain barrier (BBB),<sup>5</sup> and blood flow control.<sup>1,6</sup> Multiple lines of evidence suggest that different types of pericytes exist within distinct microvascular zones,<sup>2,3,7–9</sup> and they can be further classified by their morphology,<sup>2,8,9</sup> gene expression,<sup>10</sup> and cellular dynamics (in terms of intracellular calcium signaling<sup>11</sup> and contractility<sup>3,6,12,13</sup>). Ensheathing pericytes enwrap the vessels within 4 branches of the penetrating arteriole and express high levels of the contractile protein  $\alpha$ -smooth muscle actin ( $\alpha$ -SMA), which facilitates dynamic fluctuations in vessel diameter<sup>11–13</sup> and rapid dilation during neurovascular coupling.<sup>3</sup> Debate exists over the

<sup>1</sup>Institute of Pharmacology and Toxicology, University of Zurich, Zurich, Switzerland

<sup>2</sup>Neuroscience Center, University and ETH Zurich, Zurich, Switzerland

<sup>3</sup>College of Pharmacy, University of Manitoba, Winnipeg, MB, Canada

<sup>4</sup>Department of Neurosurgery, University Hospital Zurich, University of Zurich, Zürich, Switzerland

<sup>5</sup>Department of Biochemistry and Biophysics, University of Pennsylvania, Philadelphia, Pennsylvania, USA

<sup>6</sup>Institute for Biomedical Engineering, University of Zurich and ETH Zurich, Zurich, Switzerland

## Corresponding author:

Jillian L Stobart, College of Pharmacy, University of Manitoba, 750 McDermot Ave., Winnipeg, MB, R3E 0T5, Canada.  
Email: jillian.stobart@umanitoba.ca

nomenclature for this microvascular zone, including “precapillary arterioles”,<sup>13,14</sup> “capillaries”,<sup>3,15</sup> or the “arteriole-capillary transition region”.<sup>9,12</sup> Capillary pericytes have long thin-strand processes and are located in the higher-order capillary bed ( $\geq 5$  branches from the penetrating arteriole). These pericytes express little to no  $\alpha$ -SMA, but they can dilate<sup>11</sup> or contract<sup>16</sup> capillaries, albeit at much slower time-scales than ensheathing pericytes. Venous pericytes have shorter truncated processes compared to capillary pericytes,<sup>8,11</sup> no  $\alpha$ -SMA expression,<sup>9</sup> and are found within 4 branches of the ascending venule. Such morphological diversity in pericyte types along the arterio-venous axis suggests specialized roles for these cells within the vascular network and within the known functions of pericytes such as regulation of blood flow and BBB integrity.

During aging and in pathologies such as Alzheimer’s disease, diabetic retinopathy and arteriovenous malformations,<sup>6,17–23</sup> pericytes potentially degenerate contributing to BBB leakage, changes in vascular structure, and reduced brain blood flow. Several animal models of pericyte deficiency have been generated to recapitulate disease and to study the impact of pericyte loss on the brain vascular network. Mostly, these mouse models have a range of pericyte deficiency and were generated by modifying the platelet-derived growth factor subunit B (PDGFB)/platelet-derived growth factor receptor beta (PDGFRB) signaling axis. The *Pdgfb*<sup>ret/ret</sup> strain, lacking the retention motif on the PDGFB necessary for the binding of PDGF-BB to the extracellular matrix for optimal presentation to pericytes, shows severe pericyte loss in the brain.<sup>24,25</sup> Depending on the anatomical brain region, *Pdgfb*<sup>ret/ret</sup> mice have up to a  $\sim 75\%$  reduction in pericyte coverage<sup>5,24</sup> and enlarged capillaries particularly in the cortex and hippocampus.<sup>26</sup> Several studies have shown that pericyte loss in *Pdgfb*<sup>ret/ret</sup> mice leads to reduced BBB integrity via increased transcytosis across endothelial cells.<sup>5,26</sup> Furthermore, these mice are known to have decreased resting cortical perfusion,<sup>26</sup> but the specifics of hemodynamics and the impact that severe pericyte deficiency has on blood flow has not been determined, particularly in specific microvascular zones where distinct populations of mural cells are known to reside.

The goal of this study was to investigate whether severe pericyte deficiency in *Pdgfb*<sup>ret/ret</sup> mice influences the structure, hemodynamics, and blood oxygen concentrations in vessels across cortical Layers 1 and 2/3 located in the arteriole-capillary transition region, capillaries, and what we refer to as the capillary-venule transition where venule pericytes are known to reside. We also considered the impact of pericyte-deficiency on cortical cerebrovascular reactivity. Our findings have potential implications for cortical

pathological conditions with significant pericyte loss, such as arteriovenous malformations.

## Materials and methods

### Mice

Male and female *Pdgfb*<sup>ret/ret</sup> mice and littermate controls (*Pdgfb*<sup>ret/wt</sup>) were housed under an inverted 12-hour light/dark cycle. For two-photon imaging experiments, mice were positive for *Pdgfrb*-eGFP (Gensat.org. Tg(Pdgfrb-eGFP)JN169Gsat/Mmucd) in order to visualize the mural cells. Genotyping of *Pdgfb*<sup>ret/ret</sup> was conducted as described previously.<sup>27,28</sup> Each animal was 2–3 months of age at the time of surgery and at 3–4 months of age two-photon imaging commenced. All procedures were approved by the Canton of Zurich veterinary authorities, in accordance with the guidelines of the Swiss Animal Protection Law (Act of Animal Protection 16 December 2005 and Animal Protection Ordinance 23 April 2008) (ZH151/2017). We adhered to the ARRIVE 2.0 guidelines when reporting animal data in this study.<sup>29</sup>

### Cranial window surgery

A cranial window was prepared in two surgical procedures as previously described.<sup>27,30</sup> During the first surgery, animals were anesthetized with isoflurane (4% for induction, 1–2% for maintenance), fixed in a stereotaxic frame and an incision was made to expose the skull. The bone was cleaned and then a bonding agent (Prime & Bond, Dentsply) followed by dental cement (Coltene SYNERGEY D6 Flow) was applied and polymerized with blue light. A custom-made aluminum head post restraint was attached with dental cement. In the second surgical procedure conducted 48 to 72 hours later, the animal was anesthetized with midazolam (5 mg/kg), fentanyl (0.05 mg/kg) and medetomidine (0.5 mg/kg) to cut a craniotomy over the somatosensory cortex with a dental drill. A sapphire glass window (3×3 mm; ValleyDesign) was fixed in place with dental cement over the exposed brain. Buprenorphine (0.1 mg/kg s.c. during the day and 1 mg/kg in drinking water at night) was administered for 3 days following the surgery and animals were allowed to recover at least two weeks before imaging.

### Tail vein injection

Before the imaging procedures outlined below, mice were anesthetized with isoflurane (4% for induction, 1–2% for maintenance) and the tail vein was cannulated with a 30 G needle attached to polyurethane tubing (inner diameter 0.3 mm) with a 28 G insulin needle/syringe filled with saline.<sup>31</sup> Once the 30 G needle was

confirmed to be in the tail vein following i.v. injection of 10–20  $\mu\text{l}$  of saline, the insulin syringe was switched from the end of the cannula with a syringe containing 2.5% dextran-Texas Red (70 kDa, Molecular Probes) or  $\text{PO}_2$  probe (see below). Then, 30  $\mu\text{l}$  of dye was injected into the vein and the cannula was rinsed with saline. Animals received a maximum volume of 100  $\mu\text{l}$  i.v.

### Two-photon fluorescent imaging and analysis

Fluorescent images of pericytes and blood vessels were acquired through the cranial window of lightly anesthetized animals ( $\sim 1\%$  isoflurane) with a custom-built two-photon laser-scanning microscope<sup>32</sup> equipped with a 20 $\times$  water immersion objective (W Plan-Apochromat 20 $\times$ /1.0 DIC VIS-IR, Zeiss). GFP and Texas-red dextran were excited at 940 nm with a Ti:sapphire laser (Mai Tai; Spectra-Physics) directed by galvanometric scanners. Fluorescence emission was separated by a 560 nm dichroic mirror (BrightLine; Semrock) and detected with GaAsP photomultiplier modules (Hamamatsu Photonics) fitted with a green 520/50 nm band pass filter or a red 607/70 band pass filter. A customized version of *ScanImage* (r3.8.1; Janelia Research Campus) was used to control the microscope, which was modified to enable gating the laser output during imaging (necessary for phosphorescence lifetime imaging as outlined below).

At the beginning of each imaging session, a z-stack of images was acquired from the surface pial vessels up to  $\sim 300 \mu\text{m}$  deep in the tissue with 1–2  $\mu\text{m}$  steps in the z plane. The laser power was exponentially adjusted to account for the increasing depth in the tissue. Once the eGFP positive pericytes and branches of the vascular network were identified, high resolution (512  $\times$  512 pixels, 0.74 Hz) images were collected of each vessel as a reference. To measure vascular diameter, the galvanometric scanners were directed in a line scan bisecting the vessel at 90° perpendicular to the vessel flow at scan rates up to 1500 Hz, as has been done previously.<sup>33</sup> To measure RBC velocity and other hemodynamic parameters, the galvanometric scanners were directed in a line scan parallel to the vessel flow at scan rates up to 1500 Hz. Line scan data of diameter or RBC velocity was acquired for 30 s. Data was acquired regularly (2–3 imaging sessions per week) over several months.

Experimenters were not blinded to the genotype of the animals prior to analysis because the phenotype of *Pdgfr<sup>ret/ret</sup>* vessels (Figure 1) made the genotype readily distinguishable from the microscope images. However, the diameter and RBC line scans were processed with standard parameters for both genotypes using our semi-automated image processing tool box for MATLAB (Cellular and Hemodynamic Image

Processing Suite (CHIPS<sup>34</sup>); R2016a; MathWorks) to maintain consistency. The vessel diameter was calculated from the full-width at half maximum fluorescence signal within the line scan. A Radon transformation of the RBC streak angle in the line scan was used to approximate RBC velocity.<sup>35</sup> The RBC flux was approximated from the number of RBC streaks that crossed the line scan during the image acquisition time (cells/s). The linear density was defined as the length of space occupied by RBCs divided by the total vascular length measured in the line scan.<sup>36</sup> Vascular tube hematocrit was calculated from our two photon hemodynamic measurements of vessel radius (R; i.e. half of the diameter), the RBC flux (F); and the RBC velocity (V) as follows:<sup>37,38</sup>

$$Hct = \frac{F}{V * \pi * R^2} * MCV$$

MCV was the mean corpuscular volume of mouse RBCs which has previously been measured at 45  $\mu\text{m}^3$ .<sup>37,39</sup> We also calculated a velocity variability index (VVI) for each vessel based on Bouvy et al. (2014)<sup>40</sup> as:

$$VVI = \frac{V_{\text{max}} - V_{\text{min}}}{V_{\text{mean}}}$$

where  $V_{\text{mean}}$  was the mean velocity,  $V_{\text{max}}$  was the 95th percentile velocity, and  $V_{\text{min}}$  was the 5th percentile velocity value for each line scan.

Vascular structural analysis was conducted with *AngioTool*,<sup>40</sup> using maximum-intensity projection images of 50  $\mu\text{m}$  z-stacks of Texas Red-dextran from control and *Pdgfr<sup>ret/ret</sup>* mice. Based on the microscope parameters, the scale was set to 0.9 pixels/ $\mu\text{m}$  and all small particles were removed in *AngioTool*. Output parameters considered were: vascular area, total length of vessels, and branch index (junctions/ $\text{mm}^2$ ).

### Two-photon phosphorescence imaging for oxygen measurements

In order to measure local vascular oxygen levels, oxygen probe PtP-C343 was used as described previously.<sup>41</sup> Briefly, following i.v. injection of the probe, phosphorescence was excited by the two-photon laser at 920 nm localized to specific points within the vascular network. Each phosphorescence cycle consisted of a 10 ms train of femtosecond pulses (800 pulses), followed by a 270 ms phosphorescence photon collection period. The emitted light was detected by a highly sensitive photomultiplier tube (PMT; H10770PA-50 SEL, Hamamatsu) fitted with a 690/25 nm band pass filter. Phosphorescence lifetimes were calculated by fitting the

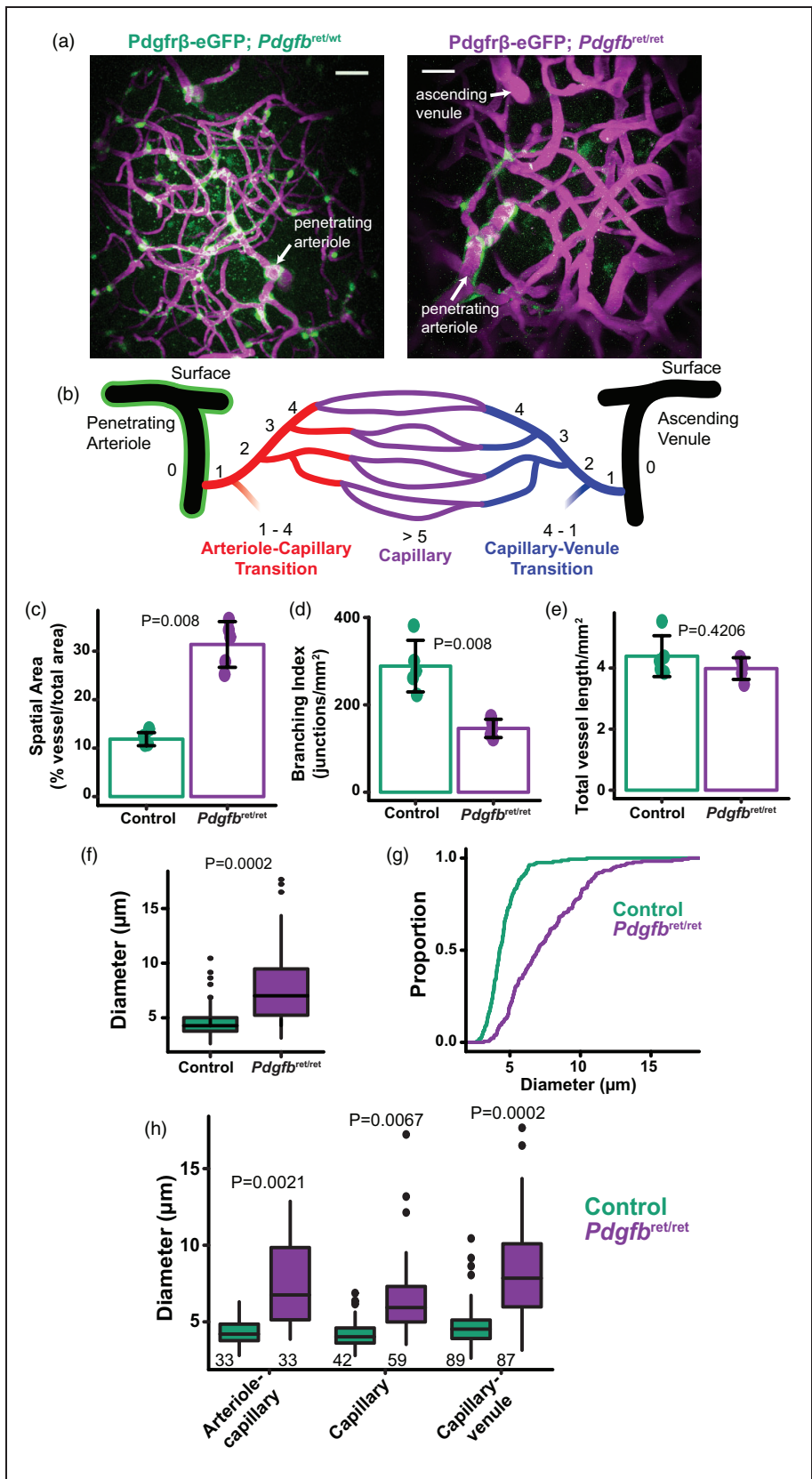


**Figure 1.** Vessel enlargement throughout the cerebrovascular network in *Pdgfr<sup>ret/ret</sup>* mice. (a) Example maximum intensity projections from a *Pdgfrβ-eGFP; Pdgfr<sup>ret/wt</sup>* mouse (Control; left) and *Pdgfrβ-eGFP; Pdgfr<sup>ret/ret</sup>* mouse (right). Blood plasma was labelled with  
Continued.



decays with single exponentials using non-linear least squares, and the standard error in the lifetimes was estimated with a bootstrap resampling approach. The lifetimes and standard errors were converted to  $PO_2$  measurements using a Stern-Volmer-like calibration plot, obtained as described previously.<sup>41</sup>

### Immunohistochemistry

Deeply anaesthetized animals were perfused for 1–2 min with PBS, followed by 5 min perfusion with 4% PFA in PBS, pH 7.2. Brains were collected and post-fixed in 4% PFA in PBS, pH 7.2 at 4°C for 6 h. Free floating brain 60  $\mu$ m coronal sections (cut with Leica VT1000S) were incubated in the blocking/permeabilization solution (1% bovine serum albumin, 0.5% Triton X-100 in PBS) overnight at 4°C, followed by incubation in primary antibody solution (0.5% bovine serum albumin, 0.25% Triton X-100 in PBS; anti-HIF1 $\alpha$  from Novusbio, Cat # NB100-479SS and anti-podocalyxin (PODXL) from R&D Systems, Cat # AF1556, dilution 1:100) for three days at 4°C, and subsequently in secondary antibody solution (donkey anti-rabbit IgG (H + L)-Cy3 Cat # 711-165-152 and donkey anti-goat IgG (H + L)-Alexa 488 #705-545-147, 1:600, Jackson ImmunoResearch) overnight at 4°C. Sections were incubated with DAPI (4',6-Diamidino-2-phenylindole dihydrochlorid) in PBS (D9542, Sigma-Aldrich, 1:10000) for 7 minutes at RT. Brain sections were mounted in ProLong Gold Antifade mounting medium (cat. #P36930, Life Technologies). Images were taken with Slidescanner Zeiss Axio Scan.Z1 (Leica Microsystems). Image processing was done using Fiji and Zen2. All images are represented as maximum intensity projections.

### Magnetic resonance imaging

Blood flow changes in 5 month old *Pdgfr<sup>ret/ret</sup>* mice and controls were measured with a pharmacological fMRI protocol as described previously.<sup>42,43</sup> Briefly, a 7/16 small animal MR Pharmascan (Bruker Biospin GmbH, Ettlingen, Germany) equipped with an actively shielded gradient set of 760 mT/m with a 80  $\mu$ s rise time was used together with a cryogenic transmitter-receiver

radiofrequency coil and operated by a Paravision 6.0 software platform. Mice were endotracheally-intubated and maintained at 1.5% isoflurane in oxygen/air (100:400 ml/min) mixture and actively ventilated at a rate of 90 breaths/minute and a tidal volume of approximately 0.3 ml/breath using a small animal ventilator (MRI-1, CWE inc. USA). The tail veins of the mice were cannulated for administration of drugs and contrast agent. A neuromuscular blocking agent, gallamine triethiodide (Sigma-Aldrich GmbH, Switzerland) was administered twice as a bolus (40  $\mu$ l, 7 mg/ml) at the beginning and before *i.v.* injection of contrast agent while the isoflurane level was reduced to 1.2%.  $T_2$ -weighted anatomical reference images were acquired using a spin echo rapid acquisition with relaxation enhancement (RARE) sequence with the same anatomical geometry as RARE sequence at pre- and post-injection of vessel dilator acetazolamide. Fifteen minutes after injection of contrast agent gallamine was injected *i.v.* (21 mg/kg body weight). Then, eight sequential pre-contrast agent scans at baseline signal intensity  $S_{pre}$  ( $CBV_0$  image) were acquired using a RARE sequence: temporal resolution = 40 s, repetition time = 3333 ms, echo time  $t_{eff}$  = 81 ms, RARE factor = 32, field-of-view = 20  $\times$  20 mm, imaging matrix = 133  $\times$  103, slice thickness = 1 mm, 1.5 mm gap, resolution = 150  $\times$  200  $\mu$ m. FLASH sequence NR = 50 was used for ensuring the successful injection of the contrast agent. After 10 repetitions, iron oxide contrast agent Endorem (50 mg Fe/kg body weight, Guerbet SA, Roissy, France) was administered *i.v.* A RARE sequence was started after five minutes after repetition = 100 and 8 averages, when the contrast agent concentration had reached steady state. After the 30th repetition (20 minutes), acetazolamide (30 mg/kg body weight; Diamox<sup>®</sup> parenteral, Goldshield Pharmaceuticals Ltd, Croydon, UK) was administered *i.v.* as a bolus. An additional 70 images were collected (46.7 minutes), yielding the image series  $S_{(t)}$ .

Image analysis was carried out using Biomap software (Novartis Institute for Biomedical Research, Basel, Switzerland). Regions of interest (ROIs) were defined for the cortex according to the mouse brain atlas by Paxinos et al. (2001).<sup>44</sup> Baseline  $CBV_0$  values  $CBV_0$  were measured for each ROI. Relative changes

#### Figure 1. Continued.

dextran-Texas Red (magenta) and mural cells expressing eGFP were visible (green). *Pdgfr<sup>ret/ret</sup>* mice have smooth muscle cells labelled with eGFP, but lack pericytes. Scale bar = 50  $\mu$ m. (b) Diagram of the cerebrovascular tree indicating the branch order for the arteriole-capillary transition zone, capillaries, and the capillary-venule transition zone. (c, d, e) Structural analysis of Z stacks from 5 *Pdgfr<sup>ret/ret</sup>* mice and 5 controls examined spatial vessel area (% vessel/total image area), branching index, and total vessel length. Dot plots are represented as mean  $\pm$  SD. Mean statistics were calculated using Mann-Whitney U tests. (f, g) Box plot and cumulative distribution plot of vessel diameters measured by line scan.  $n = 164$  vessels from 7 Control mice;  $n = 179$  vessels from 9 *Pdgfr<sup>ret/ret</sup>* mice. (e) Vessel diameters for microvascular zones: arteriole-capillary transition, capillary, and capillary-venule transition ( $n$  indicated on graphs from 7 control mice and 9 *Pdgfr<sup>ret/ret</sup>* mice). Statistics were calculated using linear mixed-effects models and Tukey post hoc tests.

of CBV in percent of prestimulation CBV values ( $\Delta CBV\%_0(t)$ ) were computed on a pixel-by-pixel basis according to Mandeville et al. (1998):<sup>45</sup>

$$\Delta CBV\%(t) = \frac{\Delta CBV(t)}{CBV_0} \times 100 = \frac{\ln((St))/\ln(S_0)}{\ln(S_0)/\ln(S_{pre})} \times 100 \quad (1)$$

$$CBV_0 = -\ln\left(\frac{T}{T_0}\right) = -\ln\left(\frac{\text{mean Post CA}}{\text{mean Pre CA}}\right) \quad (2)$$

$$\text{sqrt}(\Delta CBV\%(t)) = a \times \text{time} + b \quad (3)$$

Values for left and right sides of the brain were averaged.

### Statistics

All statistics were performed in R (version 4.1.3). Sample sizes were calculated using the `smpsize_lmm` function from the `jstats` package with a moderate effect size of 0.2, a power of 0.8, and a significance level of 0.05. Statistics for single-vessel blood flow and oxygen measurements were performed using the `lme4` package for linear mixed-effects models to account for repeated measures from the same animals. The Shapiro-Wilk test was used to test for normality. Data not normally distributed was log transformed before use in the mixed model. We used genotype (control vs *ret/ret*), microvascular zone, cortical layer and also the interaction of some pairs (e.g. genotype and cortical layer) as fixed effects. We used intercepts for individual animals as random effects. Likelihood ratio tests comparing models without fixed effects to models with fixed effects were used for the best fit while accounting for the different degrees of freedom. Residuals were plotted for visual inspection for deviations from homoscedasticity. P-values for different parameter comparisons were obtained using the `lsmeans` package with Tukey *post-hoc* tests. Statistical analysis was performed on  $\Delta CBV\%(t)$  profiles using a two-way ANOVA with Tukey *post-hoc* tests (`ggpubr` package). Mann-Whitney U tests were used for comparisons between groups when single measures from individual animals were made such as the area under the curve for  $\Delta CBV\%(t)$  profiles and vessel structural properties from `AngioTool`, as the Shapiro-Wilk test suggested these were not normally distributed.

### Software availability

CHIPS toolbox for MATLAB is freely available on GitHub (<https://ein-lab.github.io/>).<sup>34</sup> Further information and requests for resources and reagents should be

directed to and will be fulfilled by Bruno Weber ([bweber@pharma.uzh.ch](mailto:bweber@pharma.uzh.ch)).

### Results

To record resting single vessel hemodynamics at different locations of the cerebrovascular network in *Pdgfrb<sup>ret/wt</sup>* (control) and *Pdgfrb<sup>ret/ret</sup>* mice, we implanted a chronic cranial window and performed two-photon imaging of cortical blood vessels under isoflurane anesthesia (1–1.5%) following intravenous injection of 70 kDa Dextran-Texas Red (Figure 1(a)). Mice were also positive for the *Pdgfrb*-eGFP transgene to label mural cells. Previous studies found that only approximately 25% of the capillary bed is covered by pericytes in *Pdgfrb<sup>ret/ret</sup>* mice.<sup>5,26</sup> Similarly, we found *Pdgfrb<sup>ret/ret</sup>* mice had eGFP positive cells mostly on pial arteries and the penetrating arterioles with minimal labeling on all microvascular zones and ascending venules, highlighting their deficiency in pericytes (Figure 1(a)).<sup>5,25,46</sup> EGFP expression was used to distinguish penetrating arterioles from ascending venules when classifying microvascular zones as the arteriole-capillary transition region (1–4 branches from the penetrating arteriole), capillary bed ( $\geq 5$  branches from the penetrating arteriole or ascending venule) and capillary-venule transition region (1–4 branches from the ascending venule; Figure 1(b)). Maximum intensity projections of dextran Z-stack images from the cortex  $\sim 100$ – $150 \mu\text{m}$  deep were analyzed using `AngioTool` (Supplementary Fig. 1), which compared the percentage of vessel area in the total image area, the number of vessel junctions/ $\text{mm}^2$  (branching index) and the total vessel length/ $\text{mm}^2$ . *Pdgfrb<sup>ret/ret</sup>* mice had a greater vessel spatial area relative to the total image area (Figure 1(c), i.e. the vessels covered a larger field in the image) and fewer vascular branches (Figure 1(d)) compared to control mice, but the total length of vessels was the same (Figure 1(e)). The diameter of vessels in *Pdgfrb<sup>ret/ret</sup>* mice were larger than controls (Figure 1(f) and (g); *Pdgfrb<sup>ret/ret</sup>*  $7.52 \pm 2.81 \mu\text{m}$  vs. control  $4.50 \pm 1.15 \mu\text{m}$ ; mean  $\pm$  S.D.)<sup>26</sup> throughout the vascular network from the arteriole-capillary transition zone to capillaries to the capillary-venule transition region (Figure 1(b) and (h)).<sup>14</sup>

The velocity of red blood cells (RBCs) in single vessel segments was measured by line-scans parallel to the vessel, which generated kymographs with black lines for the passage of RBCs (Figure 2(a) and (b)). Overall, RBC velocities were reduced in *Pdgfrb<sup>ret/ret</sup>* mice compared to controls (Figure 2(c) and (d); *Pdgfrb<sup>ret/ret</sup>*  $0.45 \pm 0.52 \text{ mm/s}$  vs. control  $0.80 \pm 0.69 \text{ mm/s}$ ), despite larger vessel diameter (Figure 2(e)). This goes against the principle that increasing vessel diameter is associated with faster velocity,<sup>14,47,48</sup> as seen

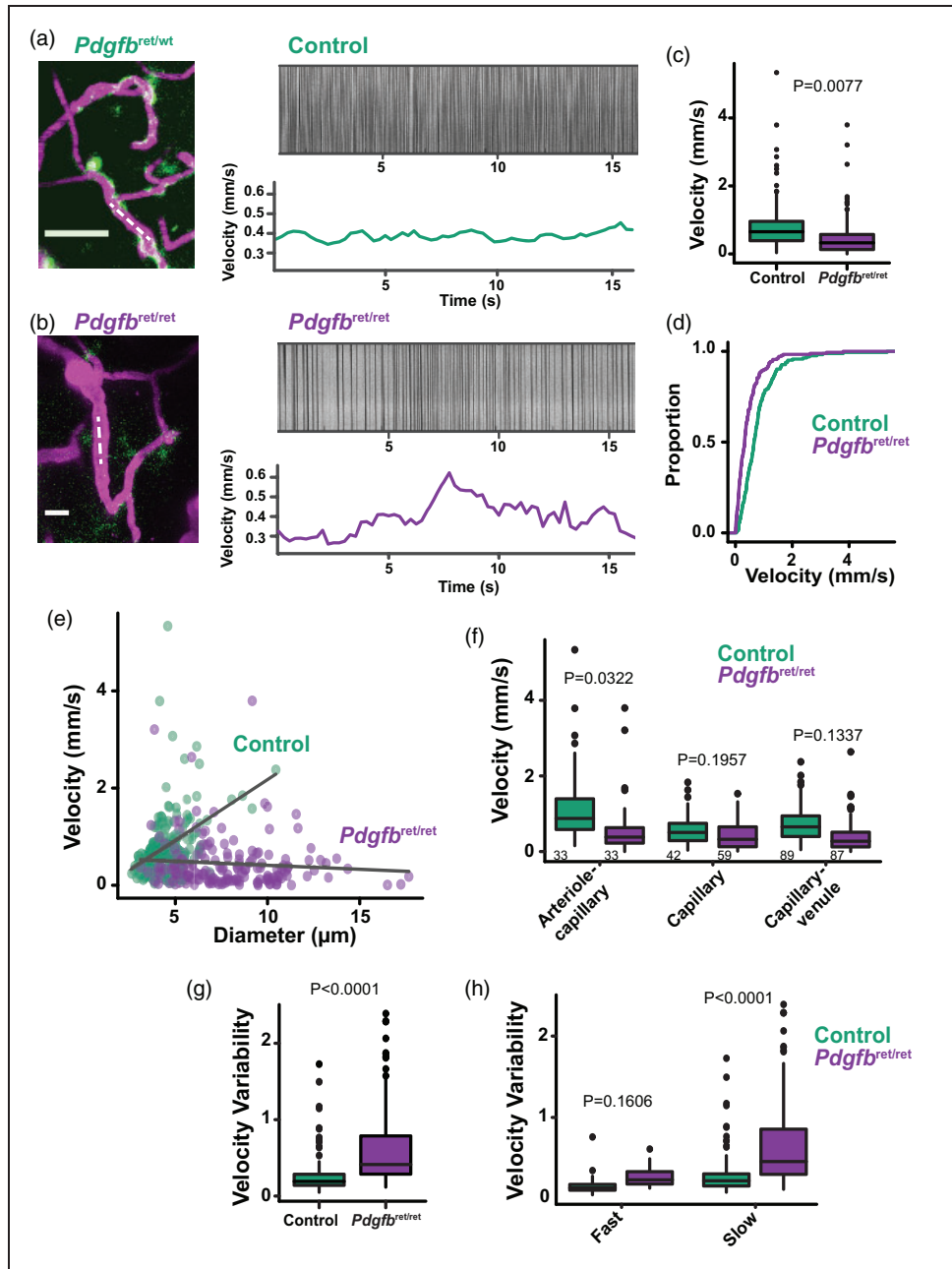


**Figure 2.** Red blood cell (RBC) velocity is reduced in *Pdgfb*<sup>ret/ret</sup> mice. (a) An example capillary network in a Control mouse (left). Line scans parallel to RBC flow (dotted line on left, kymograph top right) allows the velocity to be calculated from the streaks (bottom right). (b) An example capillary network in a *Pdgfb*<sup>ret/ret</sup> mouse (left). The RBC velocity was more variable during the scan (bottom right). (c, d) Box plot and cumulative distribution plot of RBC velocities measured by line scan.  $n = 164$  vessels from 7 Control mice;  $n = 179$  vessels from 9 *Pdgfb*<sup>ret/ret</sup> mice. (e) Scatterplot of velocity vs. diameter for each blood vessel. (f) RBC velocity at different points in the vascular tree. ( $n$  indicated on graphs from 7 control mice and 9 *Pdgfb*<sup>ret/ret</sup> mice). (g) The velocity variability index representing the dynamics or pulsatility in all vessels and (h) Slower vessels (velocity  $< 1$  mm/s) had more variable velocities. ( $n = 38$  Fast vessels and  $n = 123$  Slow vessels from 7 Control mice;  $n = 18$  Fast vessels and  $n = 160$  Slow vessels from 9 *Pdgfb*<sup>ret/ret</sup> mice). Mean statistics were calculated using linear mixed-effects models and Tukey post hoc tests.

in control animals (Figure 2(e); diameter vs. velocity Pearson's correlation coefficient for controls;  $r = 0.414$ ,  $p < 0.0001$ ; Pearson's correlation coefficient for *Pdgfb*<sup>ret/ret</sup>;  $r = -0.089$ ,  $p = 0.236$ ). The most significant reduction

in RBC velocity in *Pdgfb*<sup>ret/ret</sup> mice was observed in the arteriole-capillary transition zone covered by ensheathing pericytes, over capillaries and the capillary-venule transition area (Figure 2(f)). RBC velocities had a

higher degree of variability in *Pdgfb*<sup>ret/ret</sup> mice, often fluctuating greatly during the line scan measurements (Figure 2(b)). To capture this fluctuation, we calculated a velocity variability index<sup>49</sup>, which is the fold change in velocity relative to the mean ((max velocity-min velocity)/mean velocity). The velocity variability index was greater in *Pdgfb*<sup>ret/ret</sup> mice (Figure 2(g)), and most prominent in vessels with slower velocities (<1 mm/s; Figure 2(h)). In control mice, we also detected the occasional non-flowing or stalled blood vessel (1.2% of vessels), but only in the capillary bed. However, *Pdgfb*<sup>ret/ret</sup> mice had more frequent stalling events throughout the vascular network (8.6% of vessels from all investigated vessel zones).

We next extracted other hemodynamic properties from the line-scan analysis such as RBC flux, linear density, and tube hematocrit. Even though the RBC velocities were slower, the RBC flux (cells/s) did not differ between *Pdgfb*<sup>ret/ret</sup> mice and controls (Figure 3 (a) and (b); *Pdgfb*<sup>ret/ret</sup> 33.60 ± 32.54 cells/s vs. control 42.51 ± 34.00 cells/s), likely due to the wider overall vessel diameter in *Pdgfb*<sup>ret/ret</sup> mice. The RBC flux was also similar between genotypes within different cortical layers or microvascular zones (Supplementary Fig. 2 A, B). We calculated the linear density of RBCs as a fraction of vessel length occupied by RBCs to the total length of the line scan, and found that in *Pdgfb*<sup>ret/ret</sup> mice overall linear density was reduced (Figure 3(c) and (d); *Pdgfb*<sup>ret/ret</sup> 0.39 ± 0.16 cells/mm vs. control 0.50 ± 0.14 cells/mm), particularly in superficial cortical Layer 1, but not in specific microvascular zones (Supplementary Fig. 2 C, D). We also calculated the vascular tube hematocrit from the vessel radius, the RBC flux, and the RBC velocity<sup>37,38</sup>, assuming that the mean corpuscular volume of mouse RBCs was 45 μm<sup>3</sup>.<sup>37,39</sup> The hematocrit was lower in *Pdgfb*<sup>ret/ret</sup> mice compared to controls (Figure 3(e) and (f); *Pdgfb*<sup>ret/ret</sup> 0.13 ± 0.07 vs. control 0.23 ± 0.09 cells/mm) across all cortical layers (Figure 3(h)) and microvascular zones, but the reduction was most pronounced in capillaries and the capillary-venule transition (Figure 3(g)). Linear density and tube hematocrit have the greatest influence on efficient oxygen delivery,<sup>50</sup> so a reduction in these parameters could indicate impaired oxygen delivery in *Pdgfb*<sup>ret/ret</sup> mice.

Following this, we measured blood oxygen concentrations (PO<sub>2</sub>) in individual vessels with the phosphorescent oxygen probe, PtP-C343.<sup>51,52</sup> PO<sub>2</sub> imaging was performed at specific depths up to 200 μm into the cortex with an inter-plane distance of 25 μm. Point-based PO<sub>2</sub> measurements were acquired from penetrating arterioles, vessels in the arteriole-capillary transition, capillaries, vessels in the capillary-venule transition, and ascending venules (defined as in Figure 1(b)) from five control and five *Pdgfb*<sup>ret/ret</sup> mice (Figure 4(a)). All together, we did not detect a

difference in intravascular PO<sub>2</sub> between *Pdgfb*<sup>ret/ret</sup> mice and controls (Figure 4(b) and (c); *Pdgfb*<sup>ret/ret</sup> 41.08 ± 13.67 vs. control 39.84 ± 10.84 mmHg). A previous study of mean PO<sub>2</sub> in different cortical layers in wildtype mice found that concentrations are similar between Layer 1 and Layer 2/3,<sup>53</sup> and we made similar observations in control animals (Figure 4(d)). However, blood oxygen concentrations were higher in *Pdgfb*<sup>ret/ret</sup> mice in Layer 2/3 than Layer 1 (Figure 4(d); L1: 37.24 ± 14.26 vs. L2/3: 44.10 ± 12.36 vs mmHg). Within Layer 2/3, the capillary and capillary-venule transition zones tended to have higher oxygen concentrations in *Pdgfb*<sup>ret/ret</sup> mice compared to controls (Figure 4(e)), but this did not reach statistical significance. Nevertheless, this suggests that there could be reduced oxygen extraction from the blood leading to higher vessel concentrations in deeper cortical layers. However, we did not detect accumulation of hypoxia-inducible factor-1 alpha (HIF-1α) in the brain tissue of *Pdgfb*<sup>ret/ret</sup> mice by HIF-1α immunostaining (Supplementary Fig. 3), which suggests that resting tissue oxygen levels are stable in this mouse line.

To assess the vasoreactivity of *Pdgfb*<sup>ret/ret</sup> mice, we used vasodilator, acetazolamide<sup>54</sup>, during functional magnetic resonance imaging (fMRI). Acetazolamide injection increased cerebral blood volume (CBV) in controls and significantly less so in *Pdgfb*<sup>ret/ret</sup> mice (Figure 5(a) and (b)), which suggests an impairment in cerebrovascular reactivity in *Pdgfb*<sup>ret/ret</sup> mice.

Finally, we used male and female animals of both control and *Pdgfb*<sup>ret/ret</sup> genotypes in each experiment and we found no effect of sex on any vascular parameter measured above (diameter, velocity, pO<sub>2</sub>, etc.; data not shown). Therefore, the *Pdgfb*<sup>ret/ret</sup> mutation causes vascular dysfunction indiscriminately of sex.

## Discussion

In this study, we surveyed hemodynamics and intravascular oxygen levels in a mouse model of severe pericyte deficiency, the *Pdgfb*<sup>ret/ret</sup> strain. Compared to littermate controls, we found that the cortical vasculature in *Pdgfb*<sup>ret/ret</sup> mice was malformed, with wider vessel diameter across different microvascular zones and fewer branch junctions (Figure 1), consistent to previous histological studies with this strain.<sup>5,24</sup> These malformations contributed to slower RBC velocities that had a high degree of variability and lacked correlation between diameter and velocity which is typical in normal vascular networks (Figure 2).<sup>14,47</sup> Even though RBC velocity was reduced, there was no change in RBC flux in *Pdgfb*<sup>ret/ret</sup> mice. However, the linear density and hematocrit were decreased (Figure 3), which are critical parameters for proper oxygen diffusion to the tissue. Overall, *Pdgfb*<sup>ret/ret</sup> mice had similar mean



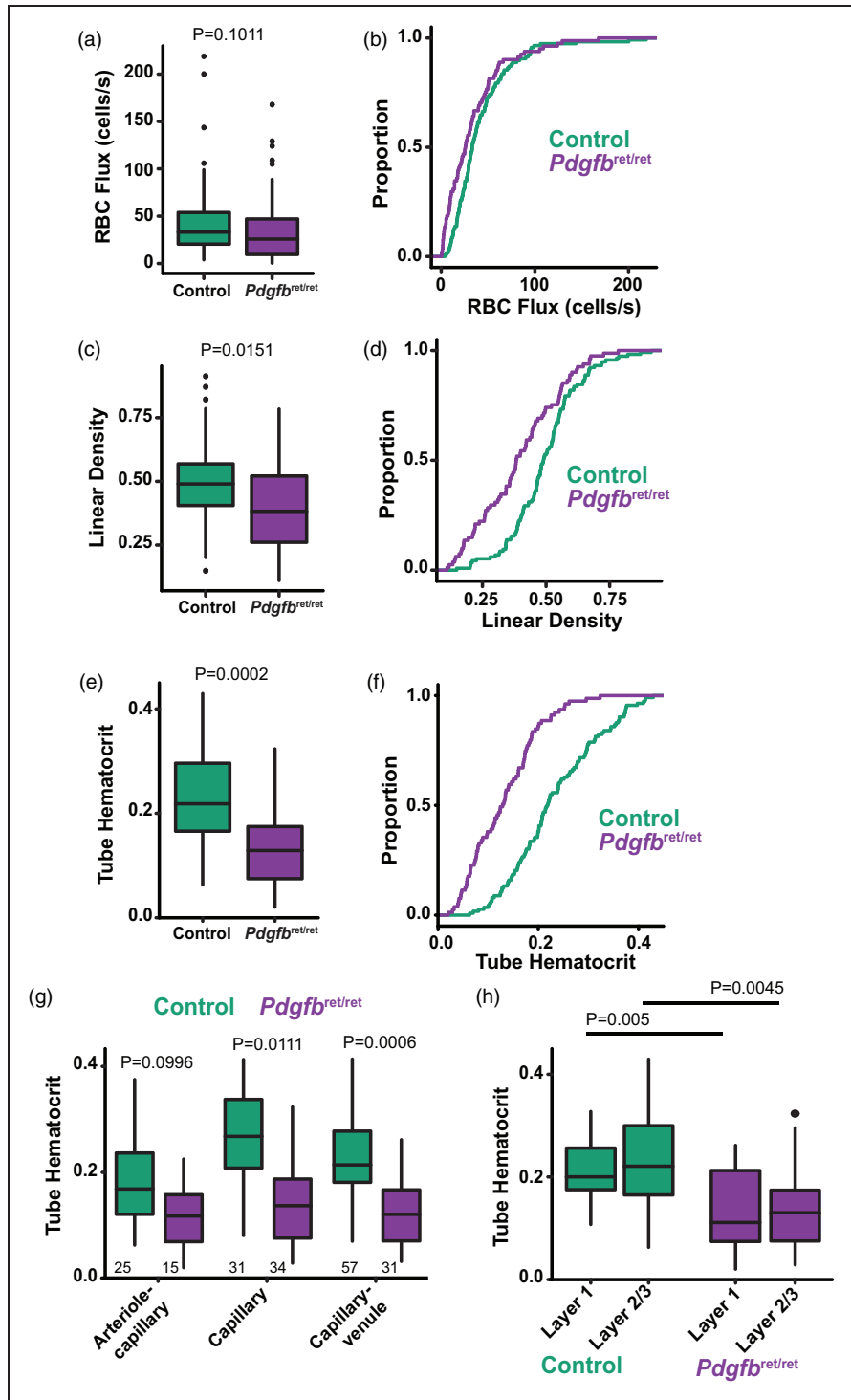


**Figure 3.** Red blood cell (RBC) density and hematocrit are reduced in *Pdgfb*<sup>ret/ret</sup> mice. (a, b) Box plot and cumulative distribution plot of RBC flux. (c, d) Box plot and cumulative distribution plot of RBC linear density. (e, f) Box plot and cumulative distribution plot of tube hematocrit. (g) Tube hematocrit in different microvascular zones and (h) Tube hematocrit in different cortical layers. N = 116 vessels from 7 Control mice; n = 81 vessels from 9 *Pdgfb*<sup>ret/ret</sup> mice for all graphs. Mean statistics were calculated using linear mixed-effects models and Tukey post hoc tests.

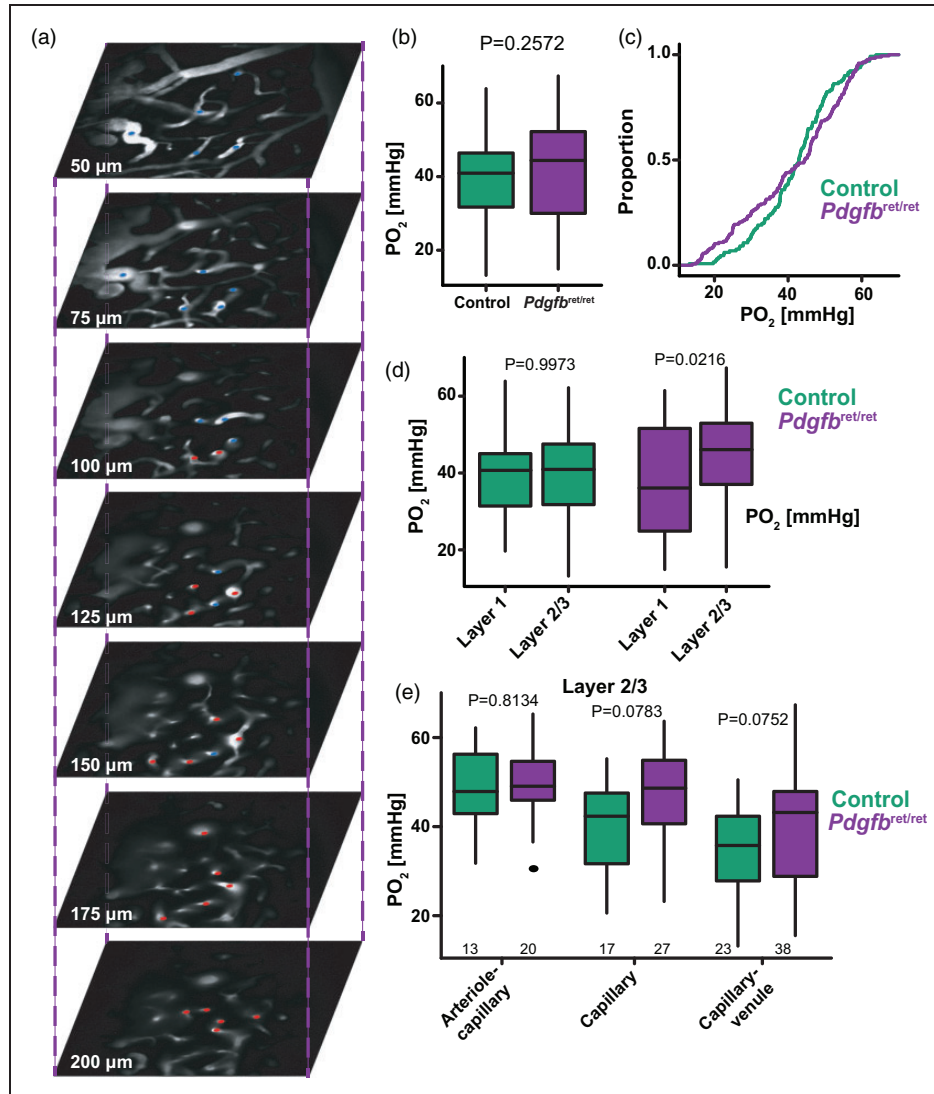


**Figure 4.** Blood oxygen levels are different between cortical layers in *Pdgfb*<sup>ret/ret</sup> mice. (a) Oxygen was measured in individual vessels at different points in the vascular tree and at different depths. Red dots indicate vessels close to the arterial side of the network, while blue dots indicate vessels on the venous side. (b, c) Box plot and cumulative distribution plot of mean intravascular oxygen levels (PO<sub>2</sub>). N = 91 vessels from 5 Control mice; n = 147 vessels from 5 *Pdgfb*<sup>ret/ret</sup> mice. (d) Box plots of PO<sub>2</sub> in cortical Layer 1 and Layer 2/3. n = 38 Layer 1 and n = 53 Layer 2/3 from 5 Control mice; n = 62 Layer 1 and n = 85 Layer 2/3 from 5 *Pdgfb*<sup>ret/ret</sup> mice and (e) Box plots of PO<sub>2</sub> in different microvascular zones within Layer 2/3. Mean statistics were calculated using linear mixed-effects models and Tukey post hoc tests.

vascular PO<sub>2</sub> to controls, but deeper vessels in layer 2/3 had higher PO<sub>2</sub> levels, suggesting reduced oxygen extraction (Figure 4). These altered hemodynamic parameters may contribute to observed impairments in cerebrovascular reactivity in *Pdgfb*<sup>ret/ret</sup> mice (Figure 5), but also changes in other critical processes such as cerebral autoregulation and neurovascular coupling that warrant further investigations.

The *Pdgfb*<sup>ret/ret</sup> model highlights the consequences on cerebrovascular structure that occur when pericyte coverage of vessels is incomplete and not present from early stages of development, which profoundly changes

the vessel diameter and branching pattern (Figure 1). Previous studies have characterized the reduced pericyte coverage in *Pdgfb*<sup>ret/ret</sup> mice by immunostaining for pericyte markers,<sup>5,24,26</sup> but details about the branch order and microvascular regions were lost in thin tissue sections. By crossing in a reporter mouse strain (*Pdgfrb*-eGFP), we are the first to report an absence of all pericyte types (ensheathing, capillary and venous pericytes) across different microvascular zones in *Pdgfb*<sup>ret/ret</sup> mice. Another model of pericyte deficiency, *Pdgfrb*<sup>+/-</sup> mice, have a progressive loss of pericytes between 27%<sup>14</sup> and 70% by 14–16 months

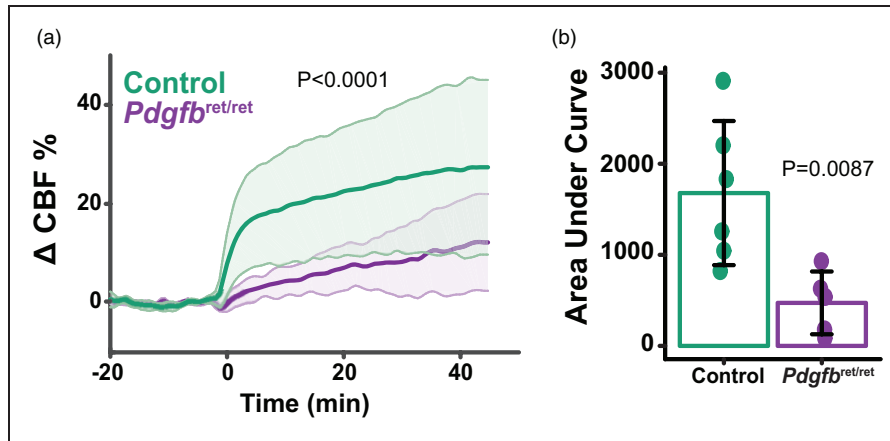


**Figure 5.** Impaired dilatory cerebral blood volume responses in *Pdgfrb<sup>ret/ret</sup>* mice by fMRI. (a) Cortical blood volume changes to acetazolamide injection (30 mg/kg; Time 0) over time. Mean  $\pm$  SD (shaded area) and (b) Area under the curve (AUC) was calculated from Time 0 until the end of scanning. Each value represents the AUC for one animal.  $n = 6$  Control mice;  $n = 5$  *Pdgfrb<sup>ret/ret</sup>* mice. Dot plot is mean  $\pm$  SD.

old.<sup>55,56</sup> It is not clear in this strain what types of pericytes are lost over time. Therefore, the *Pdgfrb<sup>ret/ret</sup>* model is perhaps better for studying pericyte deficiency at all levels of the microvascular network. The reduced vessel branching in *Pdgfrb<sup>ret/ret</sup>* mice can make it difficult to define the capillary bed because there are fewer branches in between the arterial and venous networks. Based on the branch pattern, such structure is similar to arteriovenous malformations where there is a limited capillary bed in the nidus<sup>21</sup> and pericyte-loss is commonly found.<sup>22</sup> Furthermore, mouse models with disrupted Notch signaling in pericytes develop arteriovenous malformations,<sup>57,58</sup> emphasizing a role for pericytes in this pathology.

Overall, our findings suggest *Pdgfrb<sup>ret/ret</sup>* mice are useful for studying the consequences of severe pericyte deficiency on the blood flow and vasoreactivity and show similar impairments to *Pdgfrb<sup>+/-</sup>* mice when pericyte loss has progressed to significant levels (>70%).<sup>55,56</sup> However, in terms of hemodynamics, we observed an overall reduction in RBC velocity, which was unexpected, since the vascular resistance decreases with increased vascular diameter. When fewer pericytes are lost (~27%) in *Pdgfrb<sup>+/-</sup>* mice, there is no significant change in vessel diameter, but local velocities increase, particularly in the arteriole-capillary transition region.<sup>14</sup> We also found the greatest change in velocity in this microvascular zone, highlighting the importance of this part of the vascular network for local hemodynamics, as has been shown previously.<sup>3,7,12,13</sup> When a greater number of pericytes are lost (up to 70%) in *Pdgfrb<sup>+/-</sup>* mice, capillary perfusion and neurovascular coupling responses are reduced.<sup>55,56</sup> We observed a similar reduction in cerebrovascular perfusion, particularly in reduced velocity, RBC linear

density, hematocrit, and dilatory responses to acetazolamide. Taken together, our work with *Pdgfrb<sup>ret/ret</sup>* mice and studies with *Pdgfrb<sup>+/-</sup>* mice that report a significant loss of pericytes (>70%)<sup>55,56</sup> emphasize the importance of pericytes for optimal blood flow through the vascular network.

We also found an increased incidence of stalled blood flow in *Pdgfrb<sup>ret/ret</sup>* mice. This is interesting because stalled flow in capillaries is associated with a number of pathologies, including poor reperfusion after ischemia<sup>59</sup> and Alzheimer's disease.<sup>60,61</sup> In these cases, stalled flow is caused by adhesion of neutrophils within capillaries,<sup>59-61</sup> potentially due to changes in endothelial cells and BBB integrity.<sup>61</sup> These pathologies are also associated with pericyte dysfunction or loss,<sup>6,19,20,62-64</sup> and it is tempting to speculate that a loss of pericytes as seen in *Pdgfrb<sup>ret/ret</sup>* mice may contribute to endothelial dysfunction, BBB leakage, and neutrophil adhesion that causes stalled flow in microvessels. However, a link between pericytes and stalled blood flow has not yet been determined in different disease states and we did not investigate neutrophil adhesion in *Pdgfrb<sup>ret/ret</sup>* mice. This warrants further investigation in future studies and disease models.

Previous studies have shown that RBC flux is highly correlated with mean vascular  $PO_2$ ,<sup>51-53</sup> so it is unsurprising that we did not find an overall difference in mean  $PO_2$  (Figure 4(a) to (c)) when flux (Figure 3) was the same between control and *Pdgfrb<sup>ret/ret</sup>* mice. In control mice,  $PO_2$  levels were consistent between cortical Layers 1 and 2/3, similar to a recent study.<sup>53</sup> However, blood  $PO_2$  was elevated in *Pdgfrb<sup>ret/ret</sup>* mice in Layer 2/3 compared to Layer 1, mainly in capillaries and the capillary-venule transition region (Figure 4(d))

and (e)). This suggests that *Pdgfb*<sup>ret/ret</sup> mice have less oxygen extraction from the blood. We also found that *Pdgfb*<sup>ret/ret</sup> mice had a reduced linear density and hematocrit, which is known to lead to increased intravascular resistance to oxygen transport into the tissue.<sup>50</sup> Slow RBC velocities are correlated with greater oxygen extraction,<sup>53,65</sup> so it might be expected that reduced velocity in *Pdgfb*<sup>ret/ret</sup> mice would decrease PO<sub>2</sub> across the microvascular network. However, the observed variability in velocities (Figure 2(g) and (h)) is suggestive of heterogenous, possibly non-laminar, blood flow. Oxygen extraction is facilitated by homogeneous blood flow<sup>53,66</sup> and thus, the observed variability in blood flow in *Pdgfb*<sup>ret/ret</sup> mice may also contribute to the higher PO<sub>2</sub> levels we detected in cortical Layer 2/3. Though there is potentially less oxygen extraction from the vessels in *Pdgfb*<sup>ret/ret</sup> mice, this does not cause significant tissue hypoxia in adult brain tissue at rest (no accumulation of HIF-1 $\alpha$ , was detected; Supplementary Fig. 3). However, *Pdgfb*<sup>ret/ret</sup> mice have a limited metabolic and oxygen reserve in skeletal muscle, and their performance is reduced in a physical exhaustion test.<sup>25</sup> Therefore, we expect that *Pdgfb*<sup>ret/ret</sup> mice are more likely to suffer brain hypoxia during metabolic challenges, such as ischemic stroke.

It should be noted that the *Pdgfb*<sup>ret/ret</sup> mice have increased cardiac output and heart muscle size to maintain a normal blood pressure with dilated vessels.<sup>25</sup> There is no change in resting heart rate in *Pdgfb*<sup>ret/ret</sup> mice,<sup>25</sup> so the reduced cerebral RBC velocities we observed are likely not caused by a decreased heart rate (Figure 2). Analysis of mesenteric arteries in *Pdgfb*<sup>ret/ret</sup> mice found a normal response to vasodilators and vasoconstrictors, suggesting typical resistance vessel capabilities.<sup>25</sup> However, our results with vasodilator, acetazolamide, suggest the brain has a limited capacity for increased perfusion in *Pdgfb*<sup>ret/ret</sup> mice (Figure 5). Decreased responses to acetazolamide in *Pdgfb*<sup>ret/ret</sup> mice may occur because ensheathing pericytes are lost from the arteriole-capillary transition zone. While the response of ensheathing pericytes to acetazolamide has not yet been directly studied, multiple lines of evidence suggest that these pericytes express the contractile protein machinery<sup>2,13,16</sup> for rapid changes in vessel diameter and that they are the main cells to dilate during neurovascular coupling.<sup>3,7,11,12</sup> Therefore, the reduced perfusion we observed in response to acetazolamide in *Pdgfb*<sup>ret/ret</sup> mice may occur because ensheathing pericytes that induce vasodilation within this region are lost and only smooth muscle cells on large arteries remain.

There are several limitations to this study. First, we used isoflurane anesthesia, which is known to affect neurovascular coupling<sup>67</sup> and increase mean blood PO<sub>2</sub> levels.<sup>52</sup> As a result, anesthesia may have altered

the hemodynamics and elevated the oxygen concentrations measured here. Furthermore, we did not measure blood pressure nor blood gasses such as CO<sub>2</sub> during the experiments. Blood pressure is known to be similar between *Pdgfb*<sup>ret/ret</sup> and control mice<sup>25</sup>, but nevertheless, variations in pressure and blood gasses between animals could have affected our results. Finally, we found that *Pdgfb*<sup>ret/ret</sup> mice had a deficient response to a cerebrovascular reactivity challenge, and further differences may emerge when considering other parameters such as neurovascular coupling and the response to sensory stimuli, particularly relating to oxygen consumption by the tissue.

In conclusion, *Pdgfb*<sup>ret/ret</sup> mice are a useful model to study hemodynamics of vasculature presenting a severe pericyte deficiency. These alterations in brain hemodynamics are similar to other mouse models with significant pericyte loss.<sup>55,56</sup> Pericyte loss and dysfunction is commonly reported across multiple pathologies including Alzheimer's Disease,<sup>18,19</sup> ischemic stroke<sup>6,20</sup> and diabetic retinopathy<sup>23</sup>, leading to reduced cerebral perfusion. In particular, vascular abnormalities during arteriovenous malformations are associated with pericyte-deficiency and show similarities in vascular structure to *Pdgfb*<sup>ret/ret</sup> mice (e.g. reduced branching and capillary network).<sup>21,22</sup> Future studies will provide new information about how pericyte loss and vascular malformations contribute to neurovascular coupling, vascular health, and brain circuit activity, which has potential implications for pathology, such as arteriovenous malformations.

## Funding

The author(s) disclosed receipt of the following financial support for the research, authorship, and/or publication of this article: B.W. was supported by the Swiss National Science Foundation and is a member of the Clinical Research Priority Program of the University of Zurich on Molecular Imaging. A.K. was supported by the Swiss National Science Foundation (grant 31003A\_159514, 310030\_188952) and Swiss Multiple Sclerosis Society. J.L.S. was supported by postdoctoral fellowships from the Heart and Stroke Foundation of Canada and the University of Zurich Forschungskredit. JK received funding from the Swiss National Science Foundation (320030\_179277), in the framework of ERA-NET NEURON (32NE30\_173678/1), and the Synapsis Foundation.

## Acknowledgements

We acknowledge the technical assistance of Diana Kindler.

## Declaration of conflicting interests

The author(s) declared no potential conflicts of interest with respect to the research, authorship, and/or publication of this article.



### Authors' contributions


Conceptualization, J.L.S., A.K. and B.W.; Methodology, S. V.; Software, M.J.P.B; Investigation, J.L.S., C.G., S-F.H., E. E., J.K. Y.Z. and M.L.; Formal Analysis, J.L.S., J.K. and E. E.; Writing – Original Draft J.L.S.; Writing – Review & Editing, J.L.S., C.G., E.E., A.K., and B.W.; Funding Acquisition, B.W., A.K., J.K.

### Supplementary material


Supplemental material for this article is available online.

### ORCID iDs

Jillian L Stobart  <https://orcid.org/0000-0001-7765-1408>

Chaim Glück  <https://orcid.org/0000-0002-8754-9965>

Yvette Zarb  <https://orcid.org/0000-0001-5107-0701>

Annika Keller  <https://orcid.org/0000-0003-1466-3633>

### References

- Winkler EA, Bell RD and Zlokovic BV. Central nervous system pericytes in health and disease. *Nat Neurosci* 2011; 14: 1398–1405.
- Grant RI, Hartmann DA, Underly RG, et al. Organizational hierarchy and structural diversity of microvascular pericytes in adult mouse cortex. *J Cereb Blood Flow Metab* 2019; 39: 411–425.
- Rungta RL, Chaigneau E, Osmanski B-FF, et al. Vascular compartmentalization of functional hyperemia from the synapse to the pia. *Neuron* 2018; 99: 362–375.e4.
- Coelho-Santos V, Berthiaume AA, Ornelas S, et al. Imaging the construction of capillary networks in the neonatal mouse brain. *Proc Natl Acad Sci U S A* 2021; 118: 1–12.
- Armulik A, Genové G, Mäe M, et al. Pericytes regulate the blood-brain barrier. *Nature* 2010; 468: 557–561.
- Hall CN, Reynell C, Gesslein B, et al. Capillary pericytes regulate cerebral blood flow in health and disease. *Nature* 2014; 508: 55–60.
- Zambach SA, Cai C, Helms HCC, et al. Precapillary sphincters and pericytes at first-order capillaries as key regulators for brain capillary perfusion. *Proc Natl Acad Sci U S A* 2021; 118: e2023749118.
- Hartmann DA, Underly RG, Grant RI, et al. Pericyte structure and distribution in the cerebral cortex revealed by high-resolution imaging of transgenic mice. *Neurophoton* 2015; 2: 041402.
- Hartmann DA, Coelho-Santos V and Shih AY. Pericyte control of blood flow across microvascular zones in the Central nervous system. *Annu Rev Physiol* 2022; 84: 331–354.
- Vanlandewijck M, He L, Mäe MA, et al. A molecular atlas of cell types and zonation in the brain vasculature. *Nature* 2018; 554: 475–480.
- Glück C, Ferrari KD, Binini N, et al. Distinct signatures of calcium activity in brain mural cells. *Elife* 2021; 10: 1–27.
- Gonzales AL, Klug NR, Moshkforoush A, et al. Contractile pericytes determine the direction of blood flow at capillary junctions. *Proc Natl Acad Sci U S A* 2020; 117: 27022–27033.
- Hill RA, Tong L, Yuan P, et al. Regional blood flow in the normal and ischemic brain is controlled by arteriolar smooth muscle cell contractility and not by capillary pericytes. *Neuron* 2015; 87: 95–110.
- Watson AN, Berthiaume A, Faino AV, et al. Mild pericyte deficiency is associated with aberrant brain microvascular flow in aged PDGFRbeta+/- mice. *J Cereb Blood Flow Metab* 2020; 40: 2387–2400.
- Korte N, Ilkan Z, Pearson CL, et al. The Ca<sup>2+</sup>-gated channel TMEM16A amplifies capillary pericyte contraction and reduces cerebral blood flow after ischemia. *J Clin Invest* 2022; 132: 1–17.
- Hartmann DA, Berthiaume AA, Grant RI, et al. Brain capillary pericytes exert a substantial but slow influence on blood flow. *Nat Neurosci* 2021; 24: 633–645.
- Farkas E and Luiten PGM. Cerebral microvascular pathology in aging and Alzheimer's disease. *Prog Neurobiol* 2001; 64: 575–611.
- Sagare AP, Bell RD, Zhao Z, et al. Pericyte loss influences Alzheimer-like neurodegeneration in mice. *Nat Commun* 2013; 4: 2932.
- Halliday MR, Rege SV, Ma Q, et al. Accelerated pericyte degeneration and blood-brain barrier breakdown in apolipoprotein E4 carriers with Alzheimer's disease. *J Cereb Blood Flow Metab* 2016; 36: 216–227.
- Yemisci M, Gursoy-Ozdemir Y, Vural A, et al. Pericyte contraction induced by oxidative-nitrative stress impairs capillary reflow despite successful opening of an occluded cerebral artery. *Nat Med* 2009; 15: 1031–1037.
- Winkler EA, Kim CN, Ross JM, et al. A single-cell atlas of the normal and malformed human brain vasculature. *Science* 2022; 375: 1–22.
- Winkler EA, Birk H, Burkhardt J-K, et al. Reductions in brain pericytes are associated with arteriovenous malformation vascular instability. *J Neurosurg* 2018; 129: 1–11.
- Ren J, Zhang S, Pan Y, et al. Diabetic retinopathy: involved cells, biomarkers, and treatments. *Front Pharmacol* 2022; 13: 1–21.
- Lindblom P, Gerhardt H, Liebner S, et al. Endothelial PDGF-B retention is required for proper investment of pericytes in the microvessel wall. *Genes Dev* 2003; 17: 1835–1840.
- Nyström HC, Lindblom P, Wickman A, et al. Platelet-derived growth factor B retention is essential for development of normal structure and function of conduit vessels and capillaries. *Cardiovasc Res* 2006; 71: 557–565.
- Villaseñor R, Kuennecke B, Ozmen L, et al. Region-specific permeability of the blood-brain barrier upon pericyte loss. *J Cereb Blood Flow Metab* 2017; 37: 3683–3694. 0271678X1769734.
- Stobart JL, Ferrari KD, Barrett MJPP, et al. Long-term in vivo calcium imaging of astrocytes reveals distinct cellular compartment responses to sensory stimulation. *Cereb Cortex* 2018; 28: 184–198.
- Li X, Zima AV, Sheikh F, et al. Endothelin-1-induced arrhythmogenic Ca<sup>2+</sup> signaling is abolished in atrial

- myocytes of inositol-1,4,5-trisphosphate(IP3)-receptor type 2-deficient mice. *Circ Res* 2005; 96: 1274–1281.
29. Percie Du Sert N, Hurst V, Ahluwalia A, et al. The ARRIVE guidelines 2.0: updated guidelines for reporting animal research. *J Cereb Blood Flow Metab* 2020; 40: 1769–1777.
  30. Stobart JL, Ferrari KD, Barrett MJP, et al. Cortical circuit activity evokes rapid astrocyte calcium signals on a similar timescale to neurons. *Neuron* 2018; 98: 726–735.e4.
  31. Meza-Resillas J, Ahmadpour N, Stobart M, et al. Brain pericyte calcium and hemodynamic imaging in transgenic mice in vivo. *J Vis Exp* 2021; 177: 1–17.
  32. Mayrhofer JM, Haiss F, Haenni D, et al. Design and performance of an ultra-flexible two-photon microscope for in vivo research. *Biomed Opt Express* 2015; 6: 4228–4237.
  33. Shih AY, Driscoll JD, Drew PJ, et al. Two-photon microscopy as a tool to study blood flow and neurovascular coupling in the rodent brain. *J Cereb Blood Flow Metab* 2012; 32: 1277–1309.
  34. Barrett MJP, Ferrari KD, Stobart JL, et al. CHIPS: an extensible toolbox for cellular and hemodynamic two-photon image analysis. *Neuroinformatics* 2018; 16: 145–147.
  35. Drew PJ, Blinder P, Cauwenberghs G, et al. Rapid determination of particle velocity from space-time images using the radon transform. *J Comput Neurosci* 2010; 29: 5–11.
  36. Lückner A, Secomb TW, Barrett MJP, et al. The relation between capillary transit times and hemoglobin saturation heterogeneity. Part 2: capillary networks. *Front Physiol* 2018; 9: 1–12.
  37. Santisakultarm TP, Cornelius NR, Nishimura N, et al. In vivo two-photon excited fluorescence microscopy reveals cardiac- and respiration-dependent pulsatile blood flow in cortical blood vessels in mice. *Am J Physiol Heart Circ Physiol* 2012; 302: H1367–H1377.
  38. Constantinescu AA, Vink H and Spaan JAE. Elevated capillary tube hematocrit reflects degradation of endothelial cell glycocalyx by oxidized LDL. *Am J Physiol – Hear Circ Physiol* 2001; 280: 1051–1057.
  39. O’Connell KE, Mikkola AM, Stepanek AM, et al. Practical murine hematopathology: a comparative review and implications for research. *Comp Med* 2015; 65: 96–113.
  40. Zudaire E, Gambardella L, Kurcz C, et al. A computational tool for quantitative analysis of vascular networks. *PLoS One* 2011; 6: e27385.
  41. Esipova TV, Barrett MJP, Erlebach E, et al. Oxyphor 2P: a high-performance probe for deep-tissue longitudinal oxygen imaging. *Cell Metab* 2019; 29: 736–744.e7.
  42. Mueggler T, Sturchler-Pierrat C, Baumann D, et al. Compromised hemodynamic response in amyloid precursor protein transgenic mice. *J Neurosci* 2002; 22: 7218–7224.
  43. Ni R, Kindler DR, Waag R, et al. fMRI reveals mitigation of cerebrovascular dysfunction by bradykinin receptors 1 and 2 inhibitor noscapine in a mouse model of cerebral amyloidosis. *Front Aging Neurosci* Epub ahead of print 2019; 11: 27.
  44. Paxinos G and Franklin KBJ. *Paxinos and Franklin’s the mouse brain in stereotaxic coordinates*. 2nd edn, San Diego: Academic Press, 2001.
  45. Mandeville JB, Marota JJA, Kosofsky BE, et al. Dynamic functional imaging of relative cerebral blood volume during rat forepaw stimulation. *Magn Reson Med* 1998; 39: 615–624.
  46. Török O, Schreiner B, Tsai HC, et al. Pericytes regulate vascular immune homeostasis in the CNS. *PNAS*; 118. Epub ahead of print 2021; 118: e2016587118.
  47. Desjardins M, Berti R, Lefebvre J, et al. Aging-related differences in cerebral capillary blood flow in anesthetized rats. *Neurobiol Aging* 2014; 35: 1947–1955.
  48. Li B, Lu X, Moeini M, et al. Atherosclerosis is associated with a decrease in cerebral microvascular blood flow and tissue oxygenation. *PLoS One* 2019; 14: e0221547.
  49. Bouvy WH, Geurts LJ, Kuijff HJ, et al. Assessment of blood flow velocity and pulsatility in cerebral perforating arteries with 7-T quantitative flow MRI. *NMR Biomed* 2016; 29: 1295–1304.
  50. Lückner A, Secomb TW, Weber B, et al. The relative influence of hematocrit and red blood cell velocity on oxygen transport from capillaries to tissue. *Microcirculation* 2017; 24: e12337.
  51. Lecoq J, Parpaleix A, Roussakis E, et al. Simultaneous two-photon imaging of oxygen and blood flow in deep cerebral vessels. *Nat Med* 2011; 17: 893–898.
  52. Lyons DG, Parpaleix A, Roche M, et al. Mapping oxygen concentration in the awake mouse brain. *Elife* 2016; 5: 1–16.
  53. Li B, Esipova TV, Sencan I, et al. More homogeneous capillary flow and oxygenation in deeper cortical layers correlate with increased oxygen extraction. *Elife* 2019; 8: 1–28.
  54. Vagal AS, Leach JL, Fernandez-Ulloa M, et al. The acetazolamide challenge: techniques and applications in the evaluation of chronic cerebral ischemia. *AJNR Am J Neuroradiol* 2009; 30: 876–884.
  55. Bell RD, Winkler EA, Sagare AP, et al. Pericytes control key neurovascular functions and neuronal phenotype in the adult brain and during brain aging. *Neuron* 2010; 68: 409–427.
  56. Kisler K, Nelson AR, Rege SV, et al. Pericyte degeneration leads to neurovascular uncoupling and limits oxygen supply to brain. *Nat Neurosci* 2017; 20: 406–416.
  57. Nadeem T, Bogue W, Bigit B, et al. Deficiency of notch signaling in pericytes results in arteriovenous malformations. *JCI Insight* 2020; 5: e125940.
  58. Kofler NM, Cuervo H, Uh MK, et al. Combined deficiency of Notch1 and Notch3 causes pericyte dysfunction, models CADASIL, and results in arteriovenous malformations. *Sci Rep* 2015; 5: 16449.
  59. El Amki M, Glück C, Binder N, et al. Neutrophils obstructing brain capillaries are a major cause of no-reflow in ischemic stroke. *Cell Rep* 2020; 33: 108260.
  60. Cruz Hernández JC, Bracko O, Kersbergen CJ, et al. Neutrophil adhesion in brain capillaries reduces cortical blood flow and impairs memory function in Alzheimer’s disease mouse models. *Nat Neurosci* 2019; 22: 413–420.

61. Ali M, Falkenhain K, Njiru BN, et al. VEGF signalling causes stalls in brain capillaries and reduces cerebral blood flow in Alzheimer's mice. *Brain* 2022; 145: 1449–1463.
62. Nortley R, Mishra A, Jaunmuktane Z, et al. Amyloid beta oligomers constrict human capillaries in Alzheimer's disease via signalling to pericytes. *Science* 2019; 365: eaav9518.
63. Miners JS, Schulz I and Love S. Differing associations between A $\beta$  accumulation, hypoperfusion, blood–brain barrier dysfunction and loss of PDGFRB pericyte marker in the precuneus and parietal white matter in Alzheimer's disease. *J Cereb Blood Flow Metab* 2018; 38: 103–115.
64. Sengillo JD, Winkler EA, Walker CT, et al. Deficiency in mural vascular cells coincides with blood-brain barrier disruption in Alzheimer's disease. *Brain Pathol* 2013; 23: 303–310.
65. Schmid F, Tsai PS, Kleinfeld D, et al. Depth-dependent flow and pressure characteristics in cortical microvascular networks. *PLoS Comput Biol* 2017; 13: e1005392.
66. Ostergaard L, Engedal TS, Aamand R, et al. Capillary transit time heterogeneity and flow-metabolism coupling after traumatic brain injury. *J Cereb Blood Flow Metab* 2014; 34: 1585–1598.
67. Masamoto K, Fukuda M, Vazquez A, et al. Dose-dependent effect of isoflurane on neurovascular coupling in rat cerebral cortex. *Eur J Neurosci* 2009; 30: 242–250.